East Asian Journal on Applied Mathematics
doi: 10.4208/eajam.231114.240915a

Vol. **6**, No. 1, pp. 1-22
February 2016

Integrating Feature Direction Information with a Level Set Formulation for Image Segmentation

Meng Li[1,*] and Yi Zhan[2]

[1] *Department of Mathematics, Key Laboratory of Group & Graph Theories and Applications, Chongqing University of Arts and Sciences, Yongchuan Chongqing 402160, China.*

[2] *College of Mathematics and Statistics, Chongqing Technology and Business University, Chongqing 400067, China.*

Received 23 November 2014; Accepted (in revised version) 24 September 2015

Abstract. A feature-dependent variational level set formulation is proposed for image segmentation. Two second order directional derivatives act as the external constraint in the level set evolution, with the directional derivative across the image features direction playing a key role in contour extraction and another only slightly contributes. To overcome the local gradient limit, we integrate the information from the maximal (in magnitude) second-order directional derivative into a common variational framework. It naturally encourages the level set function to deform (up or down) in opposite directions on either side of the image edges, and thus automatically generates object contours. An additional benefit of this proposed model is that it does not require manual initial contours, and our method can capture weak objects in noisy or intensity-inhomogeneous images. Experiments on infrared and medical images demonstrate its advantages.

AMS subject classifications: 65M10, 78A48

Key words: Image segmentation, level set evolution, variational model, image feature, maximal second-order directional derivative.

1. Introduction

In most computer vision applications, image segmentation is a key initial step before performing high-level tasks such as object recognition and tracking [1, 2]. For a given image, the segmentation problem is to find optimally a set of curves that partition the image domain into different regions such that each region is uniform and homogeneous in one or more characteristics (e.g., intensity, colour or texture). However, many images are characterised by intensity inhomogeneity, noise, texture and weak object, etc., which could cause

*Corresponding author. *Email address:* limeng7319@163.com (M. Li)

errors in the process of image segmentation. Various different purpose methods, including for example the thresholding algorithm [3], wavelet transformation [4], stochastic algorithm [5], graph cut [6] and variational level set models [7-10], have been proposed for these tasks. We focus on the variational level set method, which has the main advantage that it easily incorporates various prior knowledge such as on gradients and second-order directional derivatives, in formulating an energy functional for robust image segmentation.

The level set method introduced by Osher & Sethian [11] is a versatile tool for interface tracing. In image processing and computer vision applications, variational level set models have been studied extensively for image segmentation [7-10]. These variational level set models express object contour extraction as the minimisation of an energy functional, performed using gradient descent that provides a partial differential equation (PDE) for level set evolution. The zero level set (evolution curve) is used to represent the object contours, and the evolution PDE is subject to constraints from both the level set function (LSF) itself and the image data. According to the difference in constraints from the LSF, the energy functional typically includes the internal energy and external energy. The internal energy smooths the level zero curve and the LSF itself, and the external energy assists robust image segmentation.

Existing level set models for image segmentation can roughly be categorised into two classes — viz. region-based models [8, 10, 12-15] and edge-based models [7, 9, 16, 17]. Region-based models approximate the intensity in each region by global or local statistics information, and edge-based models use local edge information to construct external constraints. These models [7-10, 12-17] are amenable to physical insight into the problem of image segmentation, and build up elegant outputs via variational frameworks, especially for medical [13] and infrared images [17].

Edge-based models [7, 9] generally utilise image gradients to construct edge indicators, which are considered external constraints that stop the contours on the boundaries of the desired objects. However, the information contained in a gradient is limited to a point and its immediate neighbours, which makes the level set evolution highly sensitive to the initial contours. On the other hand, the scale value of the edge indicator is always positive, so the edge indicator cannot vanish along the object boundaries such that the curve propagating cannot stop on the object boundaries and continuously moves into weak object boundaries. In fact, an image is intrinsically a matrix that includes a large amount of data such as the intensity, gradient, or directional information and more. The data in oriented domains characterise image features such as the direction of the image edges. Incorporating the directional information into a variational framework benefits the segmentation performance of the models.

Recently, a number of algorithms incorporated image data in oriented domains into a variational framework, and attracted considerable interest [18-25]. In Ref. [18], an optimal edge-integration was designed with regard to the energy functional, which accumulates the inner product between the normal to the edge and the grey level image-gradient along the edge. Paragios *et al*. [19] proposed a bidirectional geometric flow, by integrating the gradient vector flow into the geodesic active contours (GAC) model [7] that improved the segmentation effect and exhibited more freedom with respect to the initial conditions.

In Ref. [20], a modified GAC model was proposed, where the level set evolution was controlled by an edge indicator based on the intensity profile perpendicular to the evolving front. Melonakos *et al.* [21] developed a new GAC model in a Finsler metric, where the cost of a curve is defined as the length of the curve weighted by a position and a direction, with the advantage that it allows for asymmetric processing of information. Luo & Wu [22] combined gradient directional information into the local binary fitting (LBF) model [23] for accurate image segmentation. Gallego *et al.* [24] proposed the directional GAC by accounting for the magnitude and direction of the gradient. Estellers *et al.*[25] proposed harmonic active contours, which exploit the directional information of the image gradient and the LSF, aligning the contours of the segmentation with the image edges. In preliminary work [16], we integrated the second-order directional derivatives of the image data into an external energy, which makes the variational model free of manual initialisation and produces better segmentation effects for images with complex backgrounds. However, this approach could cause an inherent ambiguity in the evolution direction of the LSF, because the external constraint is the weighted sum of two directional derivatives, which could severely damage weak object contour extractions in some noisy cases.

Here we focus on the issue of weak object segmentation with edge-based models in noisy or intensity-inhomogeneous images. We first discuss the action of the second-order directional derivatives of the image data for the level set evolution, and then propose a feature-dependent variational formulation for image segmentation. This approach is inspired by the work of Carmona & Zhong [26] with edge-based models on image smoothing and the level set method. The noise influence on the level set evolution is alleviated by removing the mistaken directive from the image contour direction. Our variational energy functional involves an external energy term and two internal energy terms. To guide the front of the active contour toward the desired object boundary, and to prevent it from moving over the weak edges in noisy images, we present a novel external energy that integrates the information in the maximal (magnitude) second-order directional derivative of the image data into a common variational framework.

The direction of the maximal second-order directional derivative is considered to be the direction across the image feature. The internal energy terms penalise the smoothing of the LSF and the deviation of the LSF from a signed distance function. The evolution of the LSF is the gradient flow that minimises the total energy functional. Due to the external energy, the level set function can be initialised as a constant function, which is more convenient than the widely used signed distance function [7, 8] or binary function [9, 10]. Our proposed model can be used to segment images with weak boundaries or intensity inhomogeneity, and it is also robust for noisy images.

In Section 2, we briefly review the work of Carmona & Zhong [26] on image smoothing and our previous work on image segmentation, and then further discuss the action of the second-order directional derivatives for level set evolution. In Section 3, our proposed new model is explained in detail. Numerical algorithms are presented in Section 4, and experimental results are given in Section 5, followed by our brief summary in Section 6.

2. Background

2.1. Image smoothing with respect to feature directions

The model proposed by Carmona & Zhong [26] respects the feature directions in image smoothing, in using the Hessian method for image feature direction extraction. For a given image $I(x,y)$, the Hessian is the matrix

$$\begin{bmatrix} I_{xx} & I_{xy} \\ I_{xy} & I_{yy} \end{bmatrix}. \tag{2.1}$$

The two eigenvalues of the Hessian are

$$\begin{aligned} \lambda_1 &= \frac{1}{2}\left(I_{xx}+I_{yy}+\sqrt{(I_{xx}-I_{yy})^2+4I_{xy}^2}\right), \\ \lambda_2 &= \frac{1}{2}\left(I_{xx}+I_{yy}-\sqrt{(I_{xx}-I_{yy})^2+4I_{xy}^2}\right). \end{aligned} \tag{2.2}$$

Let λ_η denote the larger magnitude eigenvalue and λ_ξ the other eigenvalue. The corresponding eigenvectors v_η and v_ξ can be regarded as the directions across and along the image feature, respectively. The evolution equation for the image smoothing then takes the form

$$u_t = c(a\lambda_\eta + b\lambda_\xi)\,. \tag{2.3}$$

The main idea behind this model is to control the direction of smoothing — i.e. to have minimal smoothing across the image features directions, and maximal smoothing along the image features directions.

2.2. Level set evolution without initial contours

In our previous work [16], we proposed an edge-based variational model driven by an external energy $E_{ext}(\phi)$ defined as

$$E_{ext}(\phi) = \int_\Omega w(I_\sigma) H_\varepsilon(-\phi)\,dx\,dy\,, \tag{2.4}$$

where $H_\varepsilon(\phi)$ is the smooth Heaviside function and $w(I_\sigma)$ is the weighted function defined by

$$w(I_\sigma) = g\left(|\nabla I_\sigma|\right)|\nabla I_\sigma|^2\,\frac{\partial^2 I_\sigma}{\partial \xi^2} - G'\left(|\nabla I_\sigma|\right)|\nabla I_\sigma|^2\,\frac{\partial^2 I_\sigma}{\partial \eta^2}\,, \tag{2.5}$$

involving the convolution $I_\sigma = G_\sigma * I$ of the image I with the Gaussian function G_σ (with standard deviation σ), $g(s) = 1/(1+(s/K)^2)$, $G(s) = s\cdot g(s)$, and the second-order directional derivatives $\partial^2 I_\sigma/\partial\eta^2$ and $\partial^2 I_\sigma/\partial\xi^2$ of the image I_σ along the image gradient direction η and contour direction ξ, respectively. The complete energy has two extra internal energy terms — i.e.

$$E(\phi) = E_{ext}(\phi) + \beta L(\phi) + \mu P(\phi)\,, \tag{2.6}$$

where β, $\mu > 0$ are constant, the length term $L(\phi)$ minimises the contour length, and $P(\phi)$ keeps ϕ close to the signed distance function.

In formulas (2.4)-(2.6), the weight function $w(I_\sigma)$ guides the level set function deformation in the opposite direction (up or down) on either side of the edges, so the contours can be extracted automatically at image locations that encounter two opposite directions of flow. This arrangement makes the level set evolution start with a constant level set function — i.e. this is a level set evolution model without initial contours, which we call the LSVWIC model. However, the weighted function $w(I_\sigma)$ in $E_{ext}(\phi)$ is the weighted sum of the two directional derivatives. The contour direction ξ could mistakenly give a directive to the level set evolution under some noisy circumstances and severely damage the contour extractions, a case we demonstrate in the next subsection.

2.3. Action of the second-order directional derivatives on image segmentation

If $g(s) = 1/s^2$, the function $w(I_\sigma)$ in formula (2.4) can be rewritten $w(I_\sigma) = \frac{\partial^2 I_\sigma}{\partial \xi^2} + \frac{\partial^2 I_\sigma}{\partial \eta^2}$, so the properties of $w(I_\sigma)$ have a close relationship with the Laplacian operator. It is known that the Laplacian operator has a stronger response to noise points [27], which causes an inherent ambiguity in the evolution of the LSF in noisy cases when minimising the energy (2.6). The generation of $w(I_\sigma)$ contains an external constraint in two orthogonal directions along the edge of image, one the gradient direction η and the other the contour direction ξ. To address the problem of noise sensitivity in the LSVWIC model, we must first delineate the action of $w(I_\sigma)$ in the directions ξ and η. Considering (2.5), we decompose formula (2.4) as

$$E_{ext}^{\xi}(\phi) = \int_\Omega \left(g\left(|\nabla I_\sigma|\right) |\nabla I_\sigma|^2 \frac{\partial^2 I_\sigma}{\partial \xi^2} \right) H_\varepsilon(-\phi)\, dx\, dy\,, \tag{2.7}$$

$$E_{ext}^{\eta}(\phi) = \int_\Omega \left(-G'\left(|\nabla I_\sigma|\right) |\nabla I_\sigma|^2 \frac{\partial^2 I_\sigma}{\partial \eta^2} \right) H_\varepsilon(-\phi)\, dx\, dy\,, \tag{2.8}$$

so we obtain another two models similar to (2.6) — viz.

$$E(\phi) = E_{ext}^{\xi}(\phi) + \beta L(\phi) + \mu P(\phi)\,, \tag{2.9}$$

$$E(\phi) = E_{ext}^{\eta}(\phi) + \beta L(\phi) + \mu P(\phi)\,. \tag{2.10}$$

In Fig. 1 we compare the segmentation effects of the LSVWIC model (2.6) with these modified models (2.9) and (2.10). An image with Gaussian noise of zero mean and 0.3 variance is selected to test these models — cf. Fig. 1(a). In Fig 1(b),(c) we show the segmentation results from the modified models by $E_{ext}^{\xi}(\phi)$ and $E_{ext}^{\eta}(\phi)$, respectively. It is seen that the external constraint in the contour direction ξ has little effect on the image segmentation, but the external constraint in the gradient direction η plays a key role in the level set evolution. Fig. 1(d) shows the segmentation result of the LSVWIC model. Although this model mostly still works, some false contours are generated in the resulting image, indicating that the external constraint in the contour direction ξ plays a 'bad' role in the

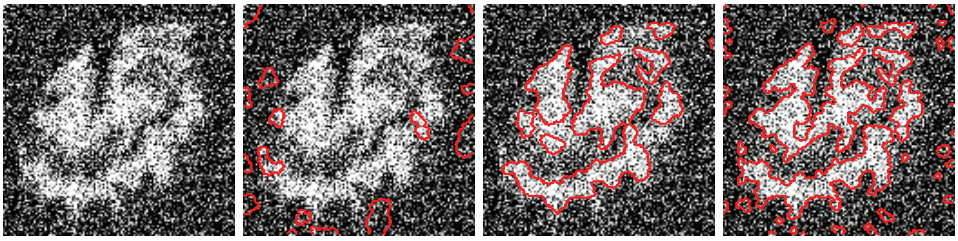

(a) (b) (c) (d)

Figure 1: An example with a noisy image: (a) noisy image; (b) result from the modified LSVWIC model with $E_{ext}^{\xi}(\phi)$ (formula (2.9)); (c) result from the modified LSVWIC model with $E_{ext}^{\eta}(\phi)$ (formula(2.10)); (d) result from the LSVWIC model (formula(2.6)).

evolution of the LSF under noisy circumstances. Thus the external constraint in the gradient direction η is better for segmentation than the weighted sum of the two directional derivatives. In fact, the directions η and ξ have a very close relationship with the direction across and along the image feature [26], and we can conclude that extraction of the image feature directions is essential to image segmentation. However, Carmona & Zhong [26] have noted that the gradient-contour (η, ξ) pair is a poor estimator across and along the feature direction pair for image smoothing. We show that this inaccurate feature direction estimation affects the segmentation results by Fig. 1 and the experiments in Section 5.

3. Proposed Model

In this section, we propose a variational model with directional information from the maximal second-order directional derivatives. Our goal is to automatically detect weak boundaries in noisy images, which depends upon accurate extraction of the image feature directions.

3.1. Integrating feature direction information to the level set

Let $\Omega \subset R^2$ be an image domain. For a given image $I : \Omega \to R$ and a level set function $\phi(x, y) : \Omega \to R$, we propose the integral

$$A_{\tilde{\lambda}}(\phi) = \int_{\Omega} \tilde{\lambda}(I(x, y)) \cdot H(-\phi)\, dx\, dy \tag{3.1}$$

as an external energy to deform the level set function and drive the zero level set toward the object boundaries, where $H(\cdot)$ is the Heaviside function and $\tilde{\lambda}(I(x, y))$ is a variable coefficient that depends upon the higher order differentiation in the Hessian matrix. When the coefficient $\tilde{\lambda}(I(x, y)) = 1$ is constant, the energy functional $A_{\tilde{\lambda}}(\phi)$ gives the area of the region $\Omega^- = \{(x, y)|\phi(x, y) < 0\}$. A positive (or negative) coefficient $\tilde{\lambda}(I(x, y))$ speeds up shrinking (or expansion) of the zero level set when minimising the energy functional (3.1) — cf. also Ref. [9]). we now specify the coefficient $\tilde{\lambda}(I(x, y))$ in detail.

On the basis of Eq. (2.1), we have the Hessian matrix of the smooth image I_σ as

$$\begin{bmatrix} (I_\sigma)_{xx} & (I_\sigma)_{xy} \\ (I_\sigma)_{xy} & (I_\sigma)_{yy} \end{bmatrix}, \tag{3.2}$$

with the two eigenvalues

$$\begin{aligned} \tilde{\lambda}_1 &= \frac{1}{2}\Big((I_\sigma)_{xx} + (I_\sigma)_{yy} + \sqrt{((I_\sigma)_{xx} - (I_\sigma)_{yy})^2 + 4(I_\sigma)_{xy}^2}\Big), \\ \tilde{\lambda}_2 &= \frac{1}{2}\Big((I_\sigma)_{xx} + (I_\sigma)_{yy} - \sqrt{((I_\sigma)_{xx} - (I_\sigma)_{yy})^2 + 4(I_\sigma)_{xy}^2}\Big). \end{aligned} \tag{3.3}$$

If $\tilde{\lambda}_\eta$ denotes the larger magnitude eigenvalue and $\tilde{\lambda}_\xi$ the other eigenvalue, depending upon the signs of $(I_\sigma)_{xx} + (I_\sigma)_{yy}$, we have

$$\tilde{\lambda}_\eta = \begin{cases} \tilde{\lambda}_1, & (I_\sigma)_{xx} + (I_\sigma)_{yy} > 0, \\ \tilde{\lambda}_2, & (I_\sigma)_{xx} + (I_\sigma)_{yy} < 0, \\ |\tilde{\lambda}_1| \text{ or } |\tilde{\lambda}_2|, & (I_\sigma)_{xx} + (I_\sigma)_{yy} = 0. \end{cases} \tag{3.4}$$

The eigenvector $\tilde{v}_\eta$ corresponding to $\tilde{\lambda}_\eta$ defines the direction of the maximal second-order directional derivative (of all directions), which is taken to be the direction across the features of the smoothing image I_σ. We write $\tilde{\lambda}(I(x,y)) = \tilde{\lambda}_\eta$, and re-write our proposed external energy (3.1) as

$$A_{\tilde{\lambda}}(\phi) = \int_\Omega \tilde{\lambda}_\eta \, H(-\phi)\, dx\, dy\,, \tag{3.5}$$

where $\tilde{\lambda}_\eta$ is defined by formula (3.4). Clearly, $\tilde{\lambda}_\eta$ shares the property of $w(I_\sigma)$ in the gradient direction η, in extracting the direction information across the image feature. However, the energy (3.5) differs from (2.4) in taking out the external constraint across the image feature direction. However, integrating $\tilde{\lambda}_\eta$ into the level set avoids the inherent ambiguity in the evolution of the LSF, and can alleviate the influence of the image noise. At the same time, the accurate directive of the maximal second-order directional derivative allows our model to capture weak objects. Let us now investigate the action of $\tilde{\lambda}_\eta$ on level set evolution by a simple example. In Fig. 2(a), the LSF ϕ evolves according to the PDE associated with $A_{\tilde{\lambda}}(\phi)$ as

$$\frac{\partial \phi}{\partial t} = \tilde{\lambda}_\eta \delta(\phi) \tag{3.6}$$

where $\delta(\phi)$ is the Dirac delta function, the derivative of the Heaviside function $H(\phi)$ introduced above, approximated by a smooth function. Fig. 2(b) shows the grey image of $\tilde{\lambda}_\eta$ about image Fig. 2(a). We see that $\tilde{\lambda}_\eta$ is positive at point A in Fig. 2(b), in the transition region associated with the dark side of the edge at point A in Fig. 2(a), and negative $\tilde{\lambda}_\eta$ associated with the bright point B in Fig. 2(b). Furthermore, from Eq. (3.6) we observe that the value of ϕ is monotone increasing if $\tilde{\lambda}_\eta > 0$, but monotone decreasing if $\tilde{\lambda}_\eta < 0$, hence the evolution processes of Eq. (3.6) in the artificial time t naturally encourage ϕ to deform (up or down) in opposite directions on either side of the image edges. We initialise

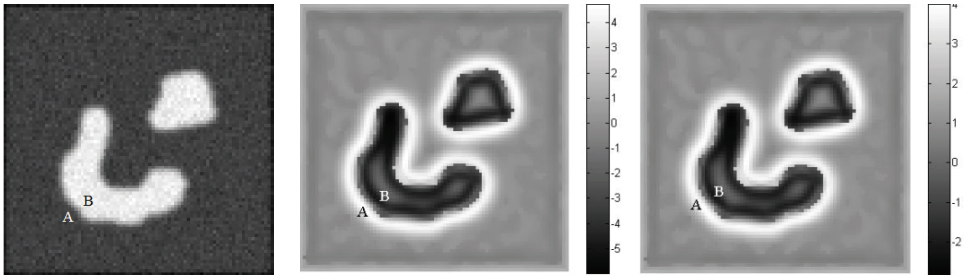

Figure 2: The grey figure of $\tilde{\lambda}_\eta$ and its contribution to level set evolution driven by Eq.(3.6): (a) original image; (b) grey figure of $\tilde{\lambda}_\eta$; (c) grey image of ϕ after one iteration.

the LSF ϕ to be a constant function with value of 1. Fig. 2(c) shows the result of ϕ after one iteration according to Eq. (3.6). We observe that the function ϕ increases from 1 to 4 in the region where $\tilde{\lambda}_\eta > 0$ (point A in Fig 2(b)) and decreases to -3 from 1 in the region where $\tilde{\lambda}_\eta < 0$ (point B in Fig 2(b)), so the contours can be generated automatically at the image locations where two opposite directions of flow are encountered after multiple iterations. This property also ensures the new scheme can be initialised as any bounded function, including a constant function.

3.2. The energy formulation

In image segmentation, the external energy $A_{\tilde{\lambda}}(\phi)$ drives the zero level set towards the desired image feature — and the internal energy, dependent only on the function of ϕ, must be defined to constrain the LSF itself. The constraints can be categorised in two parts — viz. the constraints on the zero level curve, and those on the LSF. Here we use the length term in [8, 9] in our model to constrain the smoothness of the zero level curve, and to avoid small isolated regions occurring in the final segmentation. In the sense of distributions, the length term is expressed as

$$L(\phi) = \int_\Omega |\nabla H(\phi)|\, dx\, dy = \int_\Omega \delta(\phi)\, |\nabla \phi|\, dx\, dy\,, \tag{3.7}$$

where $\delta(z)$ is the Dirac delta function. For the LSF to evolve stably, the distance regularised term in Ref.[9] is adopted in our model, to penalise the deviation of the level set function from a signed distance function. The distance regularised term is thus defined as

$$P(\phi) = \int_\Omega \frac{1}{2}(|\nabla \phi| - 1)^2\, dx\, dy\,. \tag{3.8}$$

From Eqs. (3.5), (3.7) and (3.8), the total energy is

$$\begin{aligned} E(\phi) &= \alpha A_{\tilde{\lambda}}(\phi) + \beta L(\phi) + \mu P(\phi) \\ &= \alpha \int_\Omega \tilde{\lambda}_\eta \cdot H(-\phi)\, dx\, dy + \beta \int_\Omega |\nabla H(\phi)|\, dx\, dy + \mu \int_\Omega \frac{1}{2}(|\nabla \phi| - 1)^2\, dx\, dy\,, \end{aligned} \tag{3.9}$$

where $\alpha, \beta, \mu > 0$ are constants and $\tilde{\lambda}_\eta$ is defined in (3.4). In a steepest descent dynamical scheme, minimising the energy functional (3.9) with respect to ϕ yields the gradient descent flow

$$\frac{\partial \phi}{\partial t} = \alpha \tilde{\lambda}_\eta \delta(\phi) + \beta \delta(\phi) \nabla \cdot \left(\frac{\nabla \phi}{|\nabla \phi|} \right) + \mu \left(\Delta \phi - \nabla \cdot \left(\frac{\nabla \phi}{|\nabla \phi|} \right) \right). \tag{3.10}$$

4. Implementation

4.1. Numerical scheme

In practice, the Dirac function $\delta(z)$ is approximated by a smooth function $\delta_\varepsilon(z)$, which is typically

$$\delta_\varepsilon(z) = \frac{1}{\pi} \frac{\varepsilon}{\varepsilon^2 + z^2}, \tag{4.1}$$

and we adopt $\varepsilon = 2.0$ for all of the numerical results reported here. In the numerical implementation, the spatial partial derivatives $\partial \phi / \partial x$ and $\partial \phi / \partial y$ in (3.10) are approximated by central differences, and the temporal partial derivative $\partial \phi / \partial t$ by the forward difference formula. Let Δt be the time step, h be the space step and $(x_i, y_i) = (ih, jh)$ denote the grid points. Let $\phi^n_{i,j} = \phi(x_i, y_j, n\Delta t)$ be an approximation of $\phi(x, y, t)$ for integers $n \geq 0$, and write $\phi^0 = \phi_0$. The central differences are thus

$$\Delta^x \phi_{i,j} = \frac{\phi_{i+1,j} - \phi_{i-1,j}}{2h}, \qquad \Delta^y \phi_{i,j} = \frac{\phi_{i,j+1} - \phi_{i,j-1}}{2h}, \tag{4.2}$$

and the evolution equation (3.14) is discretised as

$$\frac{\phi^{n+1}_{i,j} - \phi^n_{i,j}}{\Delta t} = \alpha \tilde{\lambda}_\eta \delta_\varepsilon(\phi^n_{i,j}) + \beta \delta_\varepsilon(\phi^n_{i,j}) k^n_{i,j} + \mu \left(\Delta^x(\Delta^x \phi^n_{i,j}) + \Delta^y(\Delta^y \phi^n_{i,j}) - k^n_{i,j} \right), \tag{4.3}$$

where

$$k^n_{i,j} = \Delta^x \left(\frac{\Delta^x \phi^n_{i,j}}{\sqrt{(\Delta^x \phi^n_{i,j})^2 + (\Delta^y \phi^n_{i,j})^2}} \right) + \Delta^y \left(\frac{\Delta^y \phi^n_{i,j}}{\sqrt{(\Delta^x \phi^n_{i,j})^2 + (\Delta^y \phi^n_{i,j})^2}} \right). \tag{4.4}$$

The computational steps are as follows;

1. initialise the level set function $\phi_0 =$ constant, and set $n = 0$;
2. compute $\tilde{\lambda}_\eta$ according to formula (3.4);
3. solve the discretised PDE (4.3), to obtain ϕ^{n+1}; and
4. check whether the evolution is stationary — if not, then set $n = n + 1$ and repeat.

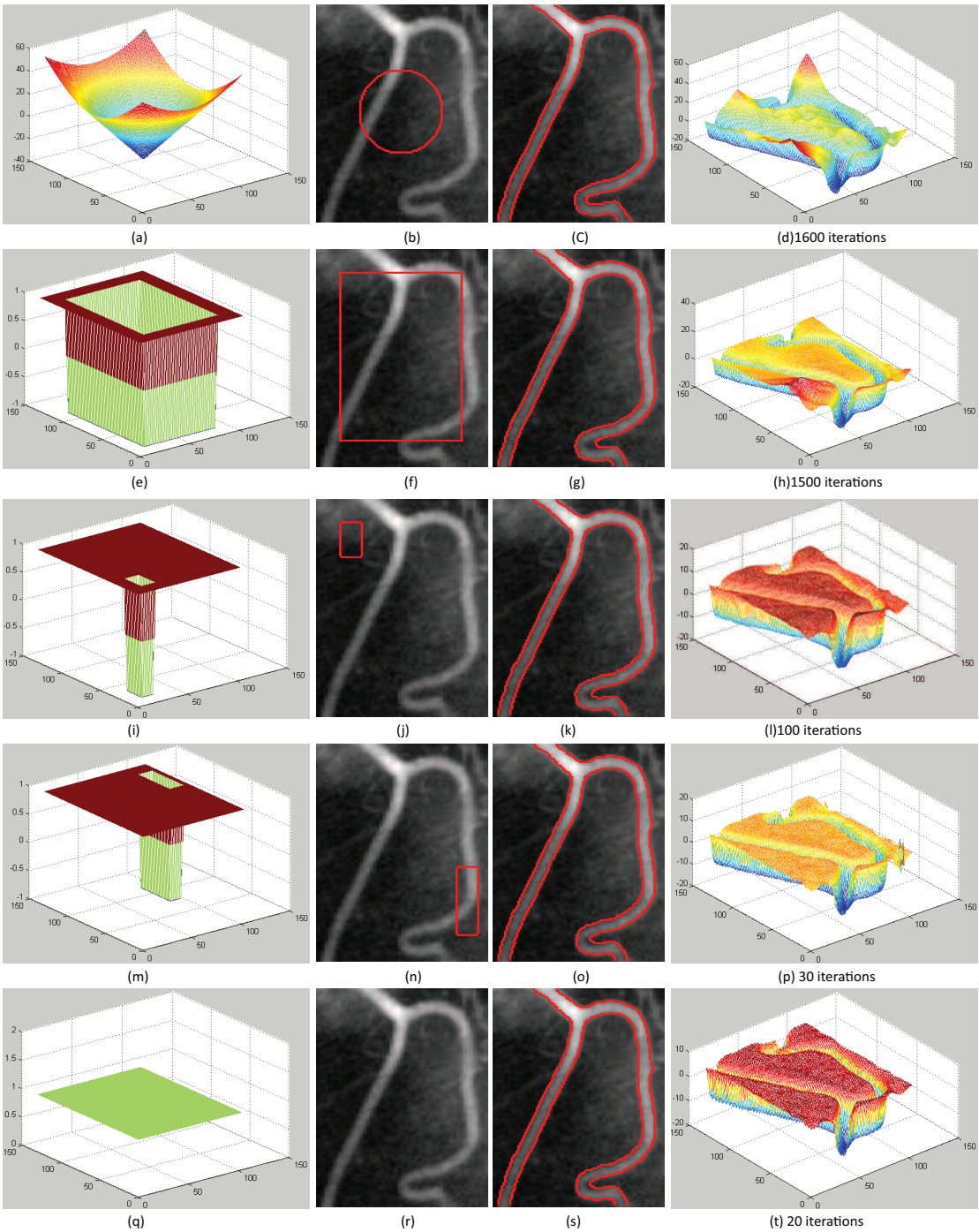

Figure 3: Segmentation of a real vessel image with different initial conditions using our proposed model. The first column: 3-D plot of initial level set functions. The second column: Initial contours correspond to different initial scheme. The third column: Finial contours of our proposed model. The forth column: 3-D plot of final level set functions.

4.2. Flexible initialisation of the level set function

In the traditional level set method, the level set function must be initialised to a singed distance function (e.g. see Refs. [7,8]) or a binary function (e.g. see Refs. [9, 10]). Since the zero level set is chosen as the starting contour for the level set evolution and the Euler-Lagrange equation involves gradient descent, different initial contours may lead to different local minima and so generate different segmentation results — i.e. the level set evolution is sensitive to initial contours. Because of the feature information (3.4) introduced, our proposed model allows us to adopt more flexible initialisation schemes.

Here, we propose the following three functions as the initial function ϕ_0

1) a signed distance function (see Fig. 3(a)),such as

$$\phi_0(x,y) = \begin{cases} -d, & (x,y) \in in(C) \\ 0, & (x,y) \in C \\ +d, & (x,y) \in out(C) \end{cases} \tag{4.5}$$

where d denotes the (shortest) Euclidean distance from the point (x,y) to the curve C.

2) a binary function(see Fig. 3(e), (i) and (m)), such as

$$\phi_0(x,y) = \begin{cases} -\rho, & (x,y) \in \omega \\ +\rho, & (x,y) \in \Omega \backslash \omega \end{cases} \tag{4.6}$$

3) a constant function (see Fig. 3(q)),such as

$$\phi_0(x,y) = \rho, \ (x,y) \in \Omega. \tag{4.7}$$

We apply the different initial schemes and evolution model (3.10) for the same image in Fig. 3. The initial contours, the evolution results and the final level set functions are shown in the second, third and forth column, respectively. As clear seen in the figures, though the level set evolution starts with different initial level set functions and different initial contours, the same desirable results are obtained. This experiment demonstrates the robustness of our model to initial conditions.

It is worth noting that the constant initialisation scheme significantly deviates from a signed distance function or a binary function. There are no initial contours for the constant initialisation scheme (see Fig. 3(q) and (r)). During the evolution, the contours emerge automatically via the image information and convergence to the object boundaries. This means that our proposed model eliminates the need of initial contours. Indeed the constant initialisation scheme makes us do not consider the problems, such as how and where to initialize the contours. So it frees of manual intervention to define the initial contours.

5. Experimental Results

This section shows the results from our proposed model for both synthetic and real images. In our numerical experiments, the LSF $\phi(x,y,t)$ is initialized as the function ϕ_0 with $\phi_0(x,y) = 1$ (for images that have brighter objects) or $\phi_0(x,y) = -1$ (for images

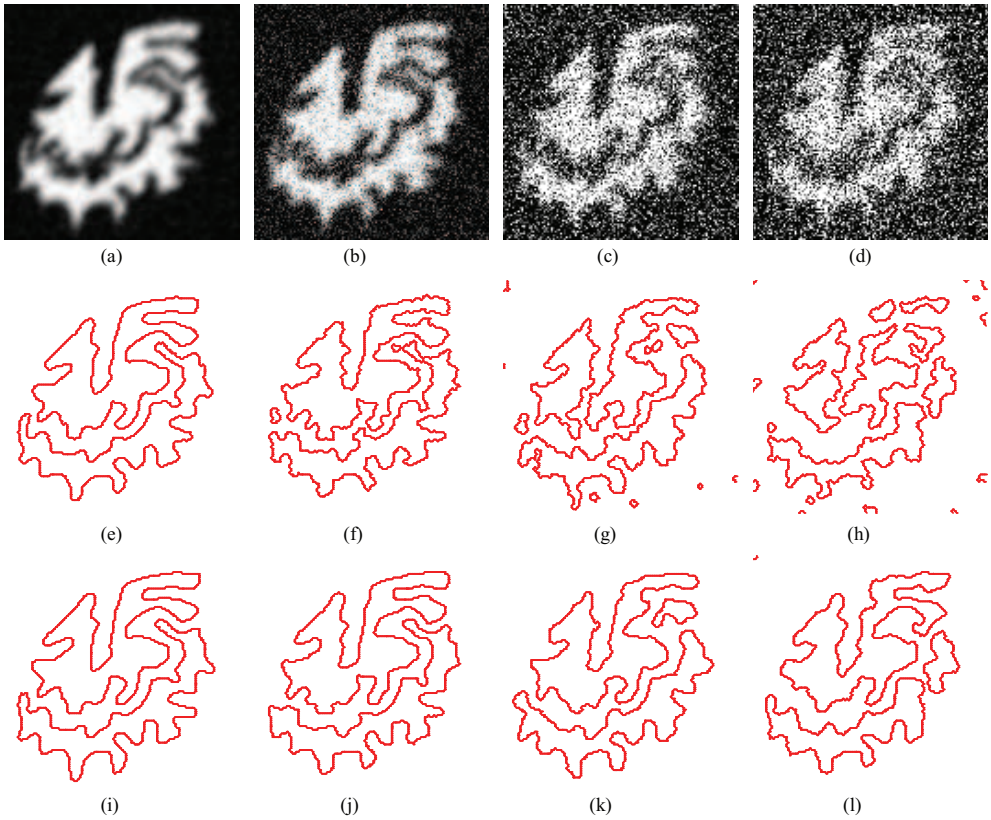

Figure 4: Comparisons of the LSVWIC model [16] and our proposed model for clean and noisy images. Row 1: clean and noisy images ((a)clean image; (b)noisy image (zero mean, 0.09 variance); (c)noisy image (zero mean, 0.2 variance); (d)noisy image (zero mean, 0.3 variance)). Row 2: results from the LSVWIC model (left to right: K = 1, 0.75, 0.70 and 0.65). Row 3: results from our proposed model (left to right: $\alpha = 2$, 1.22, 1.13 and 1.13).

that have darker objects). In addition, we choose $\sigma = 2.2$, $\beta = 10$, $\mu = 0.04$ and time step $\Delta t = 5.0$. Only the regularisation parameter α, which has a scaling role, is not the same for different experiments. If we have to detect a weak or blurry object, then α should be large. If we have to detect a object in noisy environment, then α should be small. We will give the exact value of α in each experiment, performed on Intel(R) Core(TM)i5-3317U CPU 1.70GHz with Matlab 2011, on Win7.

Fig. 4 shows the robustness of our proposed model to noisy images. In the experiment, three images are created by adding Gaussian noise to a synthetic dragon-like image (128 × 128, Fig. 4(a)), as shown in the first row. The results obtained by the LSVWIC model and our proposed method are shown in the second and third row, respectively. Results show that similar visual quality appears for the first two images. As the noise increases, some correct contours are prone to collapse, and some false contours are generated in the results from the LSVWIC model (see Fig. 4(g) and (h)). But our proposed model achieves satisfactory results for these high-level noisy images (see Fig. 4(k) and (l)).

Table 1: The DSC and RSE values for the images in Fig. 4.

	DSC			RSE		
Image	Fig.4(b)	Fig4.(c)	Fig4.(d)	Fig.4(b)	Fig4.(c)	Fig4.(d)
LSVWIC model	0.9275	0.8814	0.8192	0.0443	0.0699	0.0988
our proposed	0.9397	0.9142	0.9079	0.0369	0.0521	0.0547

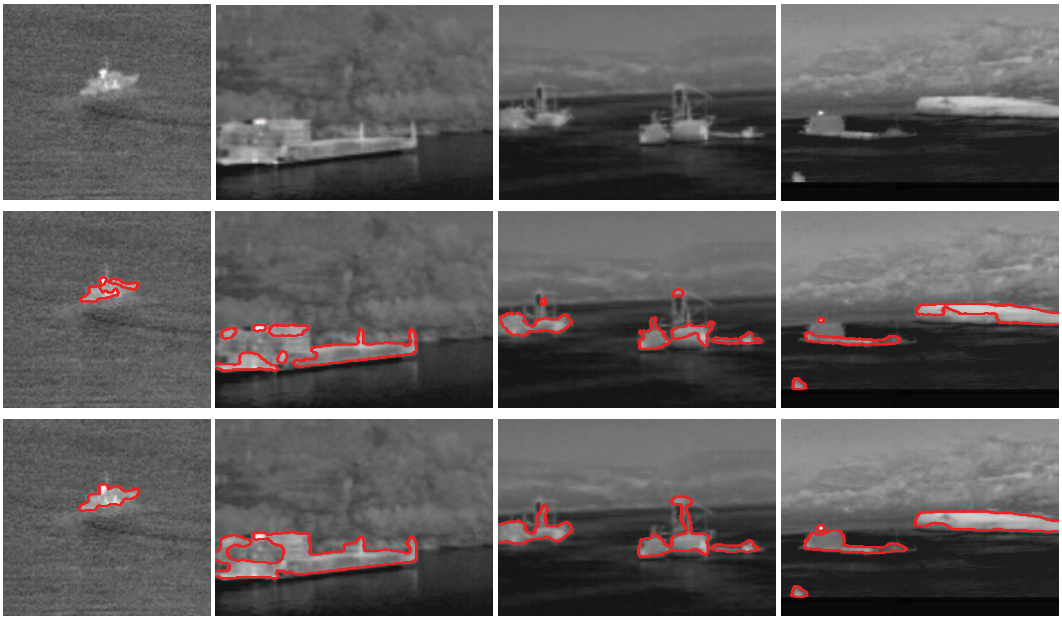

(a) (b) (c) (d)

Figure 5: Comparisons of the LSVWIC model [16] and our proposed model for infrared images with weak objects. Row 1: original images. Row 2: results from the LSVWIC model (left to right: K = 1.2, 1.0, 1.0 and 0.9). Row 3: results from our proposed model (left to right: α = 2.0, 1.6, 1.7 and 1.8).

We also demonstrate the accuracy of our proposed model by quantitative comparison. The metric adopted in this paper is the dice similarity coefficient (DSC) [28] and the segmentation error [29]. They are defined as

$$DSC = \frac{2N(S_1 \cap S_2)}{N(S_1)+N(S_2)}, \qquad RSE = \frac{N(S_2 \backslash S_1)+N(S_1 \backslash S_2)}{N(\Omega)}, \tag{5.1}$$

where $N(\cdot)$ indicates the number of pixels in the enclosed set, and Ω is the image domain. S_1 and S_2 represent the true object and the foreground region found by the model, respectively. The closer the DSC value is to 1 and the closer the RSE value is to 0, the better is the segmentation. Table 1 shows the DSC and RSE values of the LSVWIC model and our proposed model for the images in Fig. 4. The results (Fig. 4(e) and (i)) of the two models on clean image (Fig. 4(a)) are chosen as the true objects. It is clearly to know that our proposed model produces the more accurate results for these noisy images.

Figs. 5 - 7 demonstrate the effects of our proposed model on the IR images. IR images

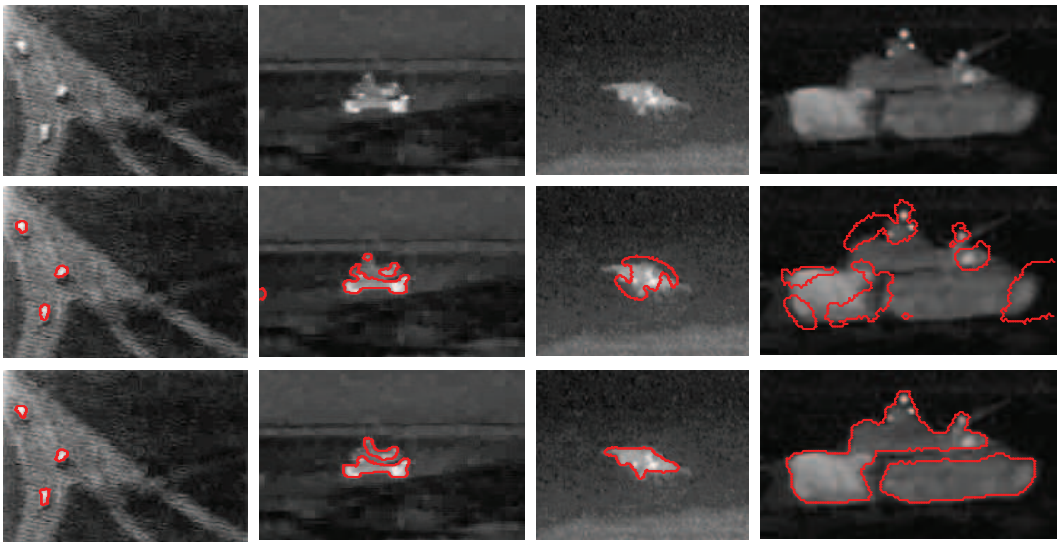

Figure 6: results from the LSVWIC model [16] and our proposed model on infrared images with blurred objects. Row 1: original images. Row 2: results from the LSVWIC model (left to right: K = 1.5, 1.7, 3.0 and 5.0). Row 3: results from our proposed model (left to right: α = 1.3, 2.5, 6.0 and 6.0).

are obtained by sensing the radiation in the IR spectrum, which is emitted or reflected by the objects in the scene. This property makes the IR images suffer from low intensity contrast with weak boundaries or noise, and difficult to detect. In Fig. 5, the LSVWIC model is compared. In the experiment, four infrared (IR) images with a water-sky background are the chosen test images, as shown in the first row in Fig. 5 (left to right: 206 × 199, 250 × 180, 250 × 180 and 319 × 232). The target is to segment the blurry boats, which are surrounded by water and sky. Both models are initialised as $\phi_0(x, y) = 1$. The second and third rows show the segmentation results from the LSVWIC model and our proposed model, respectively. We see that the LSVWIC model fails in weak object region where a boat is separated into two or more objects, but our proposed model successfully converges to the desired weak boundaries.

Fig. 6 shows the segmentation results from the LSVWIC model and our proposed model on IR images with blurred objects. The test images are shown in the first row (left to right: 196 × 145, 203 × 129, 146 × 111 and 135 × 72). We see that the targets embedded in the dim background are quite blurry. The results obtained by the LSVWIC model and our proposed method are shown in the second and third row, respectively. These results demonstrate the good performance of our proposed model in extracting blur object boundaries, unlike the results from the LSVWIC model seen in Fig. 6(b) - (d).

Fig. 7 shows our effective proposed method on various infrared images with a water-mountain-sky background (250 × 180). The wave reflection and the influence of the mountain and sky make the backgrounds of these images quite complex. The second row shows the results from the LSVWIC model. Although it extracts the objects correctly for the first two images, some false contours emerge for the last two images. The third row shows the

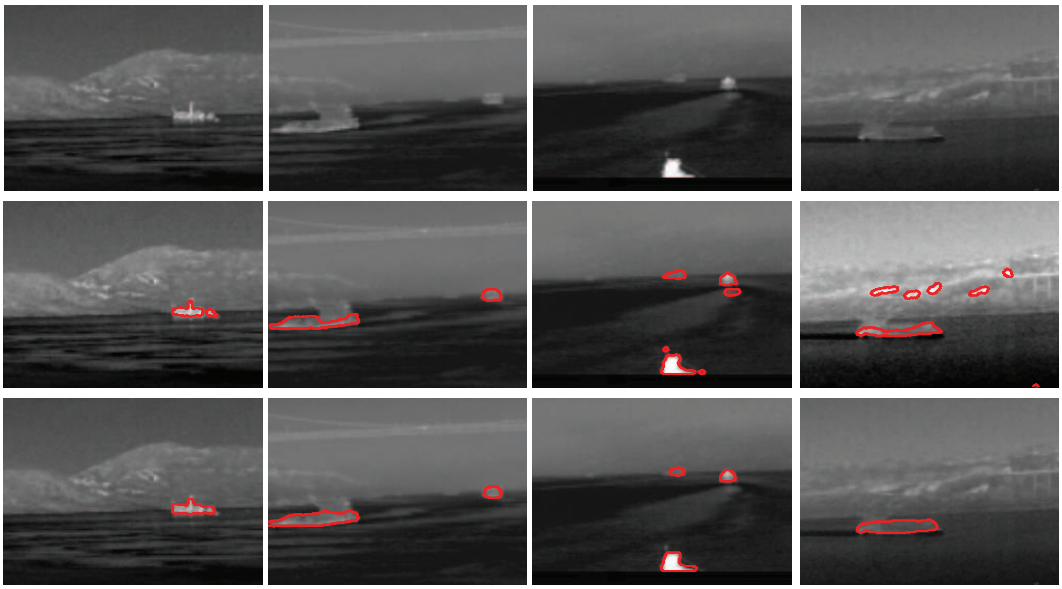

Figure 7: results from the LSVWIC model [16] and our proposed model on infrared images with water-mountain-sky background. Row 1: original images. Row 2: results from the LSVWIC model (left to right: K = 0.83, 1.0, 1.5 and 1.4). Row 3: results from our proposed model (left to right: α = 1.3, 1.5, 2.25 and 1.7).

results from our proposed model, where the object contours are extracted accurately for all images despite the scene complexity.

Figs. 8-11 illustrate the segmenting image ability of our proposed model when there is intensity inhomogeneity. Because of the technical limitation of imaging devices (e,g, the irregularities of scanner magnetic fields or non-uniform beam attenuation within the body), intensity inhomogeneity often occurs in medical images from different sources. The images have an intensity variation in the same tissue in different locations, so the segmentation is not a trivial task. Fig. 8 shows the effects of our proposed method on blood vessel images corrupted by intensity inhomogeneity, compared with the LSVWIC model and the RSF model [12]. The RSF model is a recognised widely known region-based model, with some capability to handle intensity inhomogeneity. To make a fair comparison, we chose (1) the best governing parameter ν for the RSF model, and (2) the best scale parameter K and α for the LSVWIC model and our proposed model. The test images are shown in the first row in Fig. 8. We can see that some parts of the vessels are quite weak. The second and third rows show that the RSF model with different initial contours extracts the objects correctly only for the carefully selected initial contours (in the second row), and fails to segment the objects for the other initial contours (shown in the third row), so the locations of the initial contours are crucial for the RSF model. Unlike the case of the RSF model, the level set function is initialised to a nonzero function for the LSVWIC model and our proposed model, and there is no initial contours for level set evolution. The fourth and fifth rows

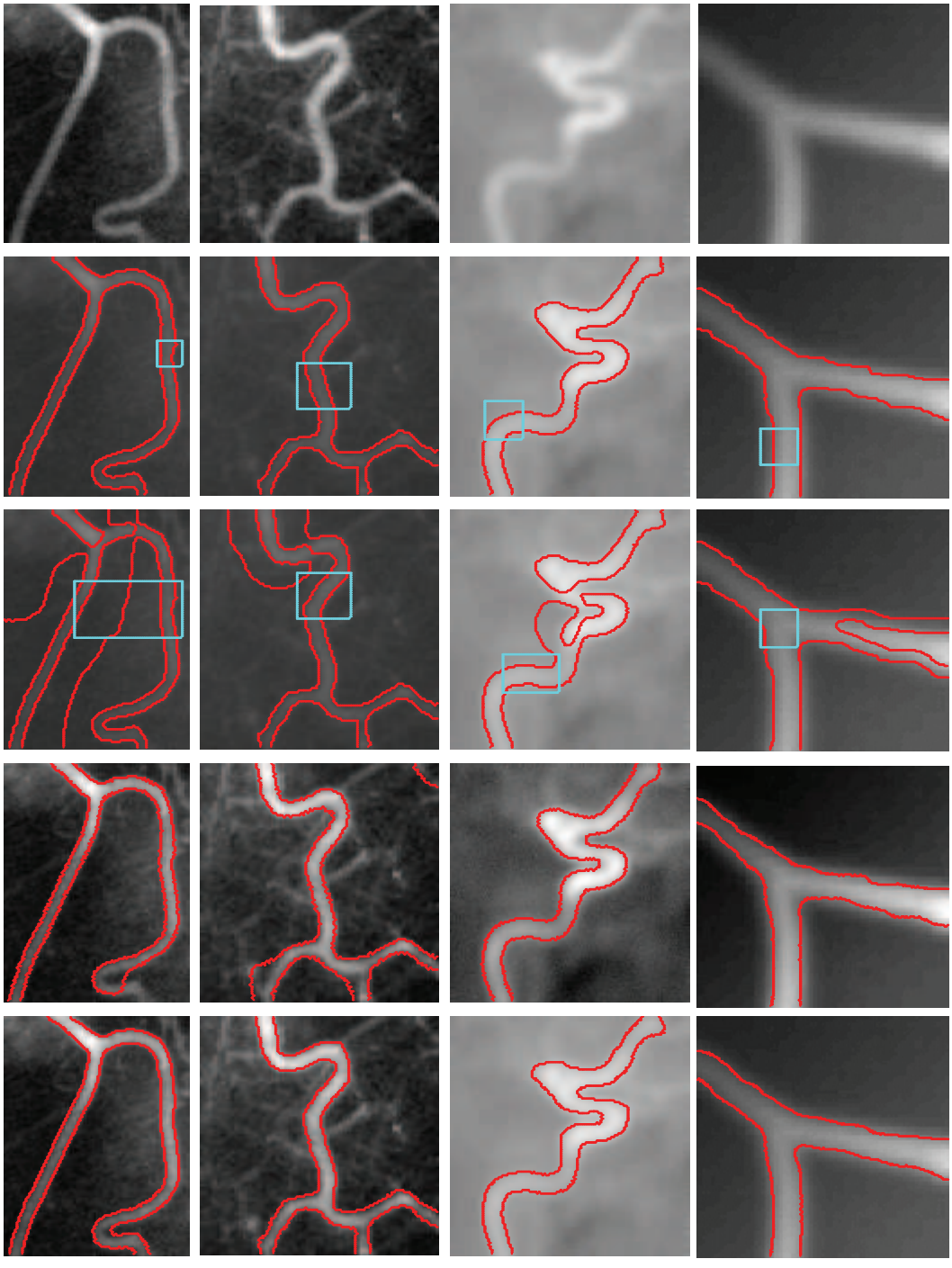

Figure 8: Results on blood vessel images. Row 1: blood vessel images. Rows 2 and 3: results from the RSF model [12] with different initial contours and with initialisations in cyan and final contours in red (left to right: $\nu = 0.001 \times 255^2$, 0.001×255^2, 0.001×255^2 and 0.0015×255^2). Row 4: results from the LSVWIC model ($K = 1.2$), starting with a constant function $\phi_0 = 0.15$. Row 5: results from our proposed model ($\alpha = 3.5$), starting with a constant function $\phi_0 = 1$.

Table 2: CPU times (in seconds) and iteration counts for the RSF, LSVWIC and our proposed model for the results shown in Fig. 8.

Image	Fig. 8(a)	Fig. 8(b)	Fig. 8(c)	Fig. 8(d)
Image size	103×131	111×110	132×131	176 ×167
RSF model	2.07 140	1.25 220	2.29 200	15.34 900
LSVWIC model	0.31 45	0.38 60	0.72 110	1.25 100
our proposed	0.23 30	0.21 30	0.26 30	0.28 20

show the results from the LSVWIC model and our proposed model, respectively. We see that the LSVWIC model cannot extract the blood vessel accurately for the first two images, but our proposed model works very well for all four images. Table 2 gives the CPU times (in seconds) and iteration counts for the three models, where both the CPU times and iteration counts for our proposed model are less than those of the RSF model and the LSVWIC model, for all four images.

Fig. 9 compares our proposed model with the LSVWIC and RSF model [12] on images with multiple weak objects. The test images shown in the first row are: a bacteria image (173 × 173), a potato image (170 × 170), a DNA channel image (229 × 168), and a cell image (176 × 169). All of these images suffer from intensity inhomogeneity. Although we made many attempts and selected the best initial contours for the RSF model, some unwanted contours were generated in the final results — cf. the second row. The third row shows that the LSVWIC model fails to segment the last image. All of the object contours were extracted correctly by our proposed model — cf. the fourth row.

Fig. 10 demonstrates the effects of our proposed method on medical images with texture background. Four breast cyst images (left to right: 91 × 92, 157 × 110, 126 × 128 and 168 × 147) were chosen as the test images, as shown in the first row. For these images, the objective of the segmentation was to extract the white cysts surrounded by breast tissues. This step is very important for computer-aided analysis in an accurate diagnosis system. However, various factors make the segmentation process more difficult — e.g. the presence of noise or hair, blurry edges, or highly asymmetric cysts,. The results show that only our proposed model accurately extracted all of the desired objects, starting with a constant function, while the RSF model and the LSVWIC model fail to segment the last three images.

Finally, we provide an experiment on more general medical images (cf. Fig. 11) to further demonstrate the performance of our proposed model. It should be noted that these images are obtained by different imaging devices. The test images in the first row are a hysterosalpingography (HSG) image (130 × 96), a vascular biopsy image (94 × 123), an MR image of corpus callosum (159 × 122) and a wrist X-ray image (90 × 196). The test images in the third row are a microscope cell image (83 × 65), an MR image of bladder (180 × 107), a brain MR image (120 × 160) and an ultrasonic image (113 × 116). The corresponding segmentation results are shown in the second and fourth rows. Although the objects in these images are quite dim and blurry, the results in the second and fourth

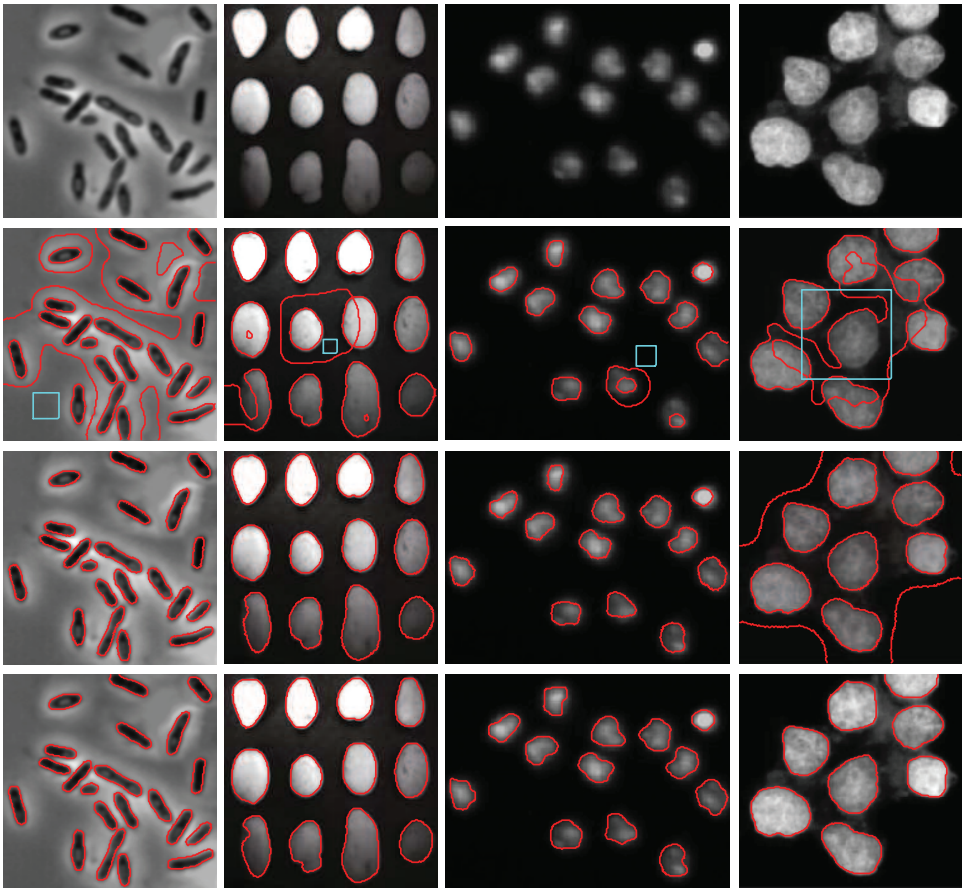

Figure 9: Results on images with multiple weak objects and intensity inhomogeneity. Row 2: results from the RSF model [12] with initialisations in cyan and final contours in red (left to right: $\alpha = 0.002 \times 255^2$, 0.001×255^2, 0.002×255^2 and 0.003×255^2). Row 3: results from the LSVWIC model (left to right: $K = 0.8$, 1, 1 and 1), starting with $\phi_0 = \rho$ (left to right: ρ = -0.15, 0.15, 0.15, and 0.15). Row 4: results from our proposed model (left to right: $\alpha = 1$, 2.5, 2.5 and 2.5), starting with $\phi_0 = \rho$ (left to right: ρ = -1, 1, 1, and 1).

rows show the desirable performance of our proposed model in segmentation.

6. Conclusion

A feature-dependent variational level set formulation for image segmentation has been discussed. Based on analysing the action of the second-order directional derivatives, we show that accurate extraction of the image feature directions is essential for the level set evolution, so the maximal eigenvalue of the second-order directional derivative is taken as a new external constraint to study. Due to good properties of the external constraint, our model can extract weak objects in noisy or intensity inhomogeneous images. The constant initialisation scheme renders our model free of manual intervention in defining the

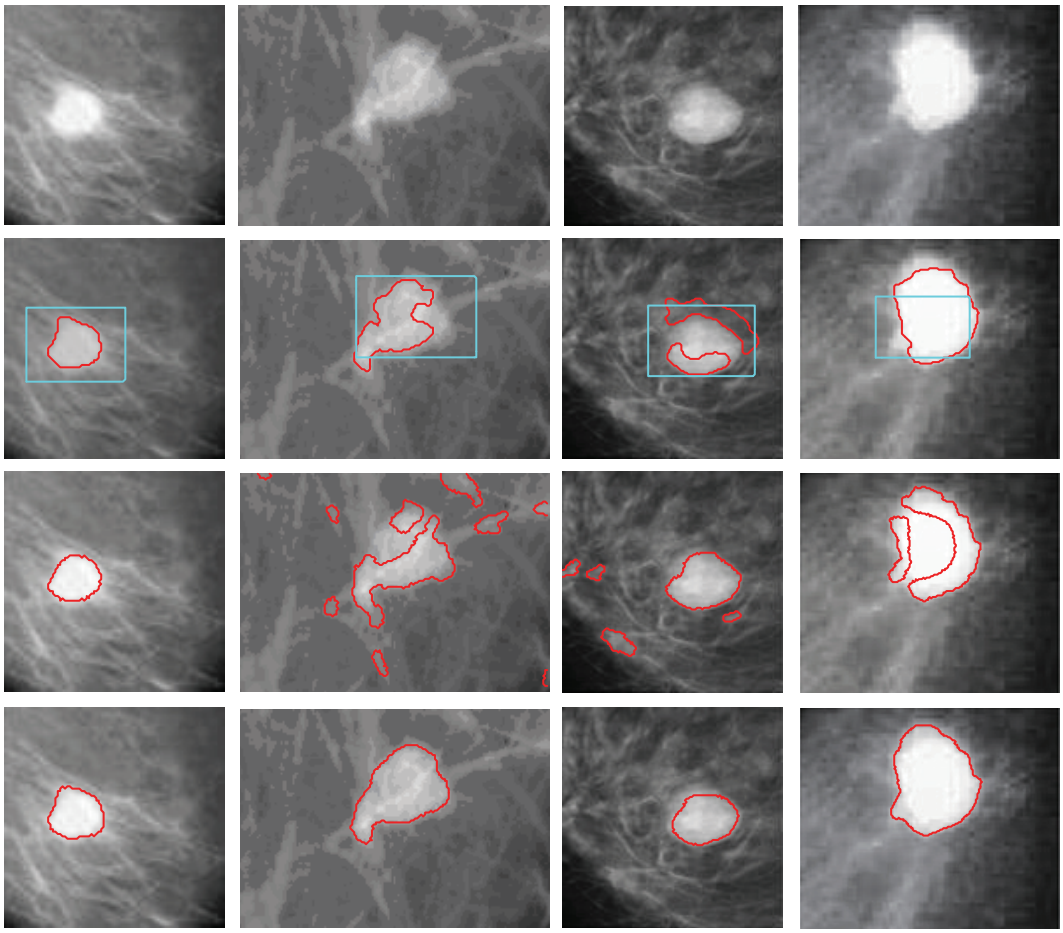

Figure 10: Results on breast cyst images that have texture background. Row 1: original images. Row 2: results from the RSF model with initialisations in cyan and final contours in red (left to right: $\nu = 0.005 \times 255^2$, 0.01×255^2, 0.005×255^2 and 0.01×255^2). Row 3: results from the LSVWIC model (left to right: $K = 0.8$, 1.5, 1.1 and 1.1), starting with $\phi_0 = 1$. Row 4: results from our proposed model (left to right: $\alpha = 1.2$, 1.4, 1.4 and 1.55), starting with $\phi_0 = 1$.

initial contours. Experiments on IR images and medical images from different modalities demonstrate the effectiveness of our proposed model.

Acknowledgments

This work is supported by the NSF of China (no. 61202349), the NSF of CQ CSTC (nos. cstc2013jcyjA40058 and cstc2015jcyjA0142), and program for innovation team building at institutions of higher education in Chongqing (no. KJTD201321).

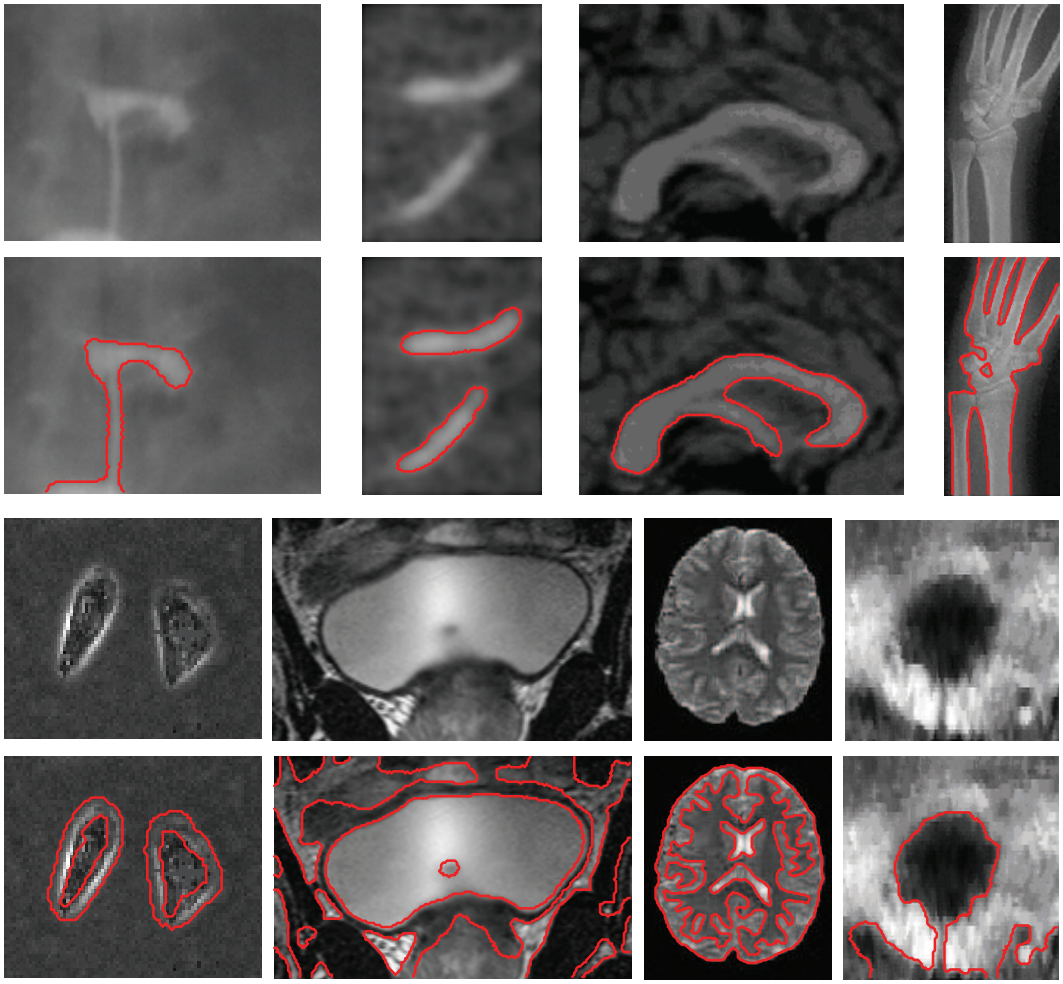

Figure 11: Results on medical images with intensity inhomogeneity. Row 1: original images; row 2: results from our proposed model (left to right: $\alpha = 2.5$, 2, 1.4 and 4), starting with a constant function $\phi_0 = \rho$ (left to right: ρ = 1, 1, 1 and -1); row 3: original images; row 4: results from our proposed model (left to right: $\alpha = 5.2$, 2, 4 and 1.2), starting with a constant function $\phi_0 = \rho$ (left to right: ρ = 1, -1, 1 and -1).

References

[1] K.E. Papoutsakis and A.A. Argyros, *Integrating tracking with fine object segmentation*, Image Vision Comp. **31**, 771-785 (2013).

[2] U. Bagci, X. Chen and J.K. Udupa, *Hierarchical scale-based multiobject recognition of 3-D anatomical structures*, IEEE Trans. Medical imaging **31**, 777-789 (2012).

[3] S. Aja-Fernández, A.H. Curiale and G. Vegas-Sánchez-Ferrero, *A local fuzzy thresholding methodology for multiregion image segmentation*, Knowledge-Based Systems **83**, 1-12 (2015).

[4] Y. Li, *Wavelet-based fuzzy multiphase image segmentation method*, Pattern Recognition Letts. **53**, 1-8 (2015).

[5] R.S. Medeiros, J. Scharcanski and A. Wong, *Image segmentation via multi-scale stochastic regional texture appearance models*, Comput. Vis. Image Und. **in press**, doi:10.1016/j.cviu.2015.06.001.

[6] Y. Yang, S. Han, T. Wang, W. Tao and X. Tai, *Multilayer graph cuts based unsupervised color-texture image segmentation using multivariate mixed student's t-distribution and regional credibility merging*, Pattern Recognition **46**, 1101-1124 (2013).

[7] V. Caselles, R. Kimmel and G. Sapiro, *Geodesic active contours*, Int. J. Comp. Vision **22**, 61-79 (1997).

[8] T. Chan and L. Vese, *Active contours without edges*, IEEE Trans. Image Proc. **10**, 266-277 (2001).

[9] C. Li, C. Xu, C. Gui and M.D. Fox, *Level set formulation without re-initialization: A new variational formulation*, in Proc. IEEE Conf. Comp. Vision Pattern Recognition (CVPR), vol. 1, pp. 430-436 (2005).

[10] Y. Wu and C. He, *A convex variational level set model for image segmentation*, Signal Processing **106**, 123-133 (2015).

[11] S. Osher and J.A. Sethian, *Fronts propagating with curvature dependent speed: Algorithms based on Hamilton-Jacobi formulations*, J. Comput. Phys. **79**.12-49 (1988).

[12] C. Li, C. Kao, J.C. Gore and Z. Ding, *Minimization of region-scalable fitting energy for image segmentation*, IEEE Trans. Image Proc. **17**, 1940-1949 (2008).

[13] C. Li, R. Huang, Z. Ding, J.C. Gatenby, D.N. Metaxas and J.C. Gore, *A level set method for image segmentation in the presence of intensity inhomogeneities with application to MRI*, IEEE Trans. Image Proc. **20**, 2007-2015 (2011).

[14] W. Zhu, X. Tai and T. Chan, *Image segmentation using Euler's elastica as the regularization*, J. Sci. Comput. **57**, 414-438 (2013).

[15] W. Liu, Y. Shang and X. Yang, *Active contour model driven by local histogram fitting energy*, Pattern Recognition Letts. **34**, 655-662 (2013)

[16] M. Li, C.J. He and Y. Zhan, *Adaptive level-set evolution without initial contours for image segmentation*, J. Electronic Imaging **20**, 023004 (2011).

[17] M. Li, C.J. He and Y. Zhan, *Tensor diffusion level set method for infrared targets contours extraction*, Infrared Phys. & Tech. **55**, 19-25 (2012).

[18] R. Kimmel, and A.M. Bruckstein, *Regularized Laplacian zero crossings as optimal edge integrators*, Int. J. Comp. Vision **53**, 225-243 (2003).

[19] N. Paragios, O. Mellina-Gottardo and V. Ramesh, *Gradient vector flow fast geometric active contours*, IEEE Trans. Pattern Anal. Machine Intelligence **26**, 402-407 (2004).

[20] I. Ersoy, F. Bunyak, M.A. Mackey and K. Palaniappan, *Cell segmentation using hessian-based detection and contour evolution with directional derivatives*, in: 15th IEEE Int. Conf. Image Proc. (ICIP), San Diego, pp. 1804-1807 (2008).

[21] J. Melonakos, E. Pichon, S. Angenent and A. Tannenbaum, *Finsler active contours*, IEEE Trans. Pattern Anal. Machine Intelligence **30**, 412-423 (2008).

[22] Z. Luo and J. Wu, *The integration of directional information and local region information for accurate image segmentation*, Pattern Recognition Letts. **32**, 1990-1997 (2011).

[23] C. Li, C. Kao, J.C. Gore and Z. Ding, *Implicit active contours driven by local binary fitting energy*, in Proc. IEEE Conf. Comp. Vision Pattern Recognition (CVPR), IEEE Computer Society, Washington, DC, pp. 1-7 (2007).

[24] G. Gallego, J.I. Ronda and A. Valdés, *Directional geodesic active contours*, in 19th IEEE Int. Conf. Image Proc. (ICIP), Orlando, pp. 2561-2564 (2012).

[25] V. Estellers, D. Zosso, X. Bresson and J. Thiran, *Harmonic active contours*, IEEE Trans. Image Proc. **23**, 69-82 (2014).

[26] R.A. Carmona, and S. Zhong, *Adaptive smoothing respecting feature directions*, IEEE Trans. Image Proc. **7**, 353-358 (1998).
[27] R.C. Gonzalez and R.E. Woods, *Digital Image Processing*, Second Edition. Prentice-Hall, New Jersey (2002).
[28] D.W. Shattuck, S.R. Sandor-Leahy, K.A. Schaper, D.A. Rottenberg and R.M. Leahy, *Magnetic resonance image tissue classification using a partial volume model*, NeuroImage **13**, 856-876 (2001).
[29] B. Liu, H.D. Cheng, J. Huang, J. Tian, X. Tang and J. Liu, *Probability density difference-based active contour for ultrasound image segmentation*, Pattern Recognition **43**, 2028-2042 (2010).